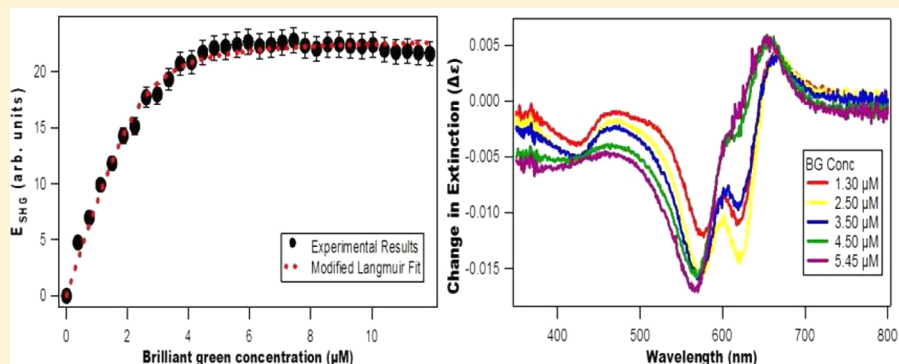


# Molecular Adsorption and Resonance Coupling at the Colloidal Gold Nanoparticle Interface

Tony E. Karam and Louis H. Haber\*

Department of Chemistry, Louisiana State University, Baton Rouge, Louisiana 70803, United States

Supporting Information



**ABSTRACT:** Second harmonic generation is used to investigate the adsorption properties of malachite green, brilliant green, and methyl green to the surface of 80 nm colloidal gold nanoparticles capped with mercaptosuccinic acid in water. The experimental results are fit using the modified Langmuir model to obtain the free energies of adsorption and the adsorbate site densities for each cationic triphenylmethane molecular dye. Malachite green is observed to bind more strongly than brilliant green or methyl green to the nanoparticle surface but has a lower adsorbate site density, indicating differences in image-charge effects, adsorbate–adsorbate repulsions, and adsorption tilt angles. Complementary measurements from extinction spectroscopy show plasmonic and molecular resonance coupling leading to the formation of new polaritonic states and Fano-type resonances with corresponding plasmon and molecular spectral depletions as the adsorbate concentration is increased. The changes in the resonance coupling spectra are compared to the second harmonic generation molecular adsorption results and demonstrate the sensitivity of plasmonic–molecular interactions.

## 1. INTRODUCTION

Gold nanoparticles are of great interest for potential applications in molecular sensing, catalysis, and biologically relevant technologies due to their chemical, electronic, and optical properties.<sup>1–9</sup> The localized surface plasmon resonances from coherent oscillations of the free electrons<sup>10–12</sup> depend on the gold nanoparticle size, shape, and surrounding medium and can lead to significant optical field enhancements for processes such as surface-enhanced Raman scattering (SERS)<sup>13,14</sup> and surface-enhanced fluorescence.<sup>15,16</sup> Nonlinear optical signals such as second harmonic generation (SHG) and sum frequency generation (SFG) are also significantly enhanced due to the nanoparticle plasmon resonance.<sup>17–24</sup> However, more information on the surface properties of colloidal metal nanoparticles and their interactions with different molecules is essential for the development and optimization of these emerging technological applications.<sup>1–5</sup>

Second harmonic generation spectroscopy constitutes a powerful technique for the investigation of the surface properties and interfacial chemistry of colloidal gold nanoparticles.<sup>25</sup> In SHG, two incident photons of frequency  $\omega$  add coherently to produce a photon of frequency  $2\omega$ . While SHG is

typically forbidden in bulk media that possess a center of inversion symmetry, SHG can be generated at interfaces such as a nanoparticle surface, making it a surface-specific nonlinear spectroscopic method for studying colloidal nanoparticle samples.<sup>26</sup> Recent SHG research has studied TiO<sub>2</sub> micro-particles,<sup>27</sup> liposomes,<sup>28</sup> carbon black,<sup>29</sup> and noble metal nanoparticles of gold, silver, and gold–silver alloys.<sup>19,21,30,31</sup> By measuring the SHG signal from a colloidal nanoparticle sample as a function of a bulk molecular adsorbate and by fitting the results to a modified Langmuir isotherm model, the free energy of adsorption and the adsorbate site density can be determined.<sup>32</sup> Related SHG characterizations of colloidal nanoparticles using  $\chi^{(3)}$  measurements can be used to obtain the surface charge densities<sup>33</sup> and acid–base equilibrium constants<sup>34</sup> at the nanoparticle surface.

In addition, interactions between plasmonic nanoparticles and organic adsorbates can give rise to molecular and plasmonic resonance coupling, which can be measured by

Received: October 12, 2013

Revised: December 10, 2013

Published: December 16, 2013

extinction spectroscopy.<sup>35</sup> When the nanoparticle plasmon resonance is degenerate with the molecular resonance, a strong coupling can occur leading to the formation of new quantum mechanical states described by a coupled-oscillator Hamiltonian resulting in new exciton-plasmon polariton peaks separated by a Rabi splitting energy.<sup>36</sup> This strong, resonant coupling has been investigated recently in organic molecular dyes interacting with silver nanoparticles on a substrate,<sup>37</sup> noble metal nanovoids,<sup>38</sup> and gold nanorods in colloidal suspension.<sup>35</sup> Fano-type resonances have also been observed in plasmonic nanostructures and metamaterials<sup>39–41</sup> and have been investigated computationally<sup>42,43</sup> from the interference of localized molecular excited states with a plasmonic continuum leading to the characteristic asymmetric line shape.<sup>44</sup> In general, more work is needed to correlate molecular and plasmonic resonance coupling with precise, surface-specific adsorption measurements that accurately account for the adsorption properties of different molecular dyes to a plasmonic nanoparticle sample.

In this paper, SHG is used to monitor the adsorption isotherms of malachite green, brilliant green, and methyl green to the surface of 80 nm colloidal gold nanoparticles capped with mercaptosuccinic acid (MSA) in aqueous suspension. The free energies of adsorption and the number of adsorbate sites per nanoparticle are determined for each molecule by fitting the experimental results to the modified Langmuir model. The molecular adsorption properties are shown to be highly dependent on the adsorbate molecular structure as well as the environment of the nanoparticle surface. In addition, complementary measurements from visible extinction spectroscopy show the formation of new exciton–plasmon polariton peaks and Fano-type profiles from resonance coupling which overlap with plasmon and molecular spectral depletions and are highly sensitive to the molecular interactions with the plasmonic gold nanoparticles.

## 2. EXPERIMENTAL SECTION

**2.1. Nanoparticle Synthesis and Characterization.** The colloidal gold nanoparticle sample is prepared by seeded growth using hydroquinone reduction, followed by thiolation and dialysis.<sup>45–47</sup> All chemicals are purchased from Sigma-Aldrich and used without further purification in ultrapure water. For the synthesis of gold nanoparticle seeds, 900  $\mu\text{L}$  of 34 mM sodium citrate is added to 30 mL of 290  $\mu\text{M}$  gold chloride in water under boiling and vigorous stirring conditions. The colloidal solution undergoes a color change from pale yellow to bright red after 10 min and is removed from heat and cooled to room temperature. For the seeded growth of the 80 nm gold nanoparticles, 100  $\mu\text{L}$  of 29 mM gold chloride and 50  $\mu\text{L}$  of the prepared gold colloidal seeds are added to 9.7 mL of water, followed by the addition of 25  $\mu\text{L}$  of 34 mM sodium citrate and 100  $\mu\text{L}$  of 0.03 M hydroquinone under vigorous stirring at room temperature. The solution is left stirring at room temperature for 60 min. The synthesis is repeated until a total of 150 mL of the 80 nm colloidal gold nanoparticle solution is produced. The nanoparticle solution is dialyzed against a solution of 22 mM mercaptosuccinic acid in water for 3 days and then against nanopure pure water for an additional 3 days in order to first attach the MSA capping agent and then to remove excess salts and reactants.

Transmission electron microscopy (TEM), extinction spectroscopy, and dynamic light scattering are used to characterize the gold nanoparticle sample. Figure 1 shows a representative TEM image of the gold nanoparticle sample. After surveying

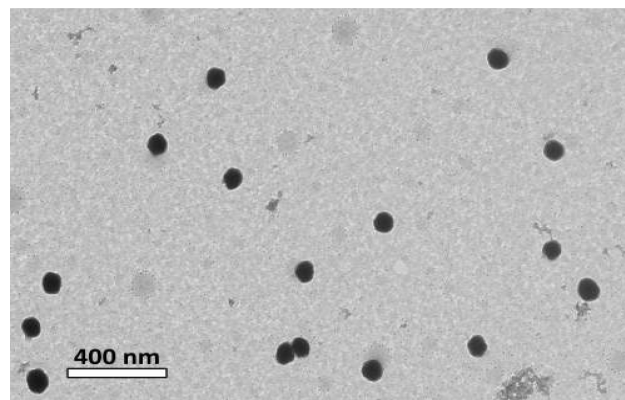


**Figure 1.** Transmission electron microscopy image of gold nanoparticles on a carbon-coated copper grid. After analysis of 500 particles, the nanoparticle diameter is determined to be  $80.0 \pm 6.1$  nm.

over 500 particles, the nanoparticle diameter is determined to be  $80 \pm 6$  nm. Figure 2 shows the extinction spectrum of the

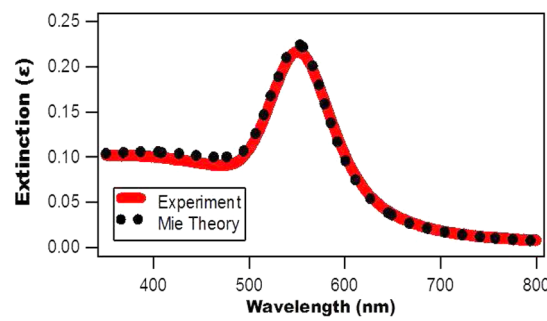


**Figure 2.** Extinction spectrum of 80 nm colloidal gold nanoparticles diluted in water (red line) overlapped with the best fit using Mie Theory (dotted black line) at a concentration of  $6.8 \times 10^8$  nanoparticles/mL.

nanoparticle solution. The 80 nm gold nanoparticles have significant scattering and absorption contributions to the overall extinction spectra. The localized surface plasmon resonance peak is observed at a center wavelength of 550 nm. The spectrum generated by Mie theory for 80 nm gold nanoparticles in water shows good agreement with the measured extinction spectrum and indicates that the stock sample concentration is  $4.1 \times 10^9$  nanoparticles/mL. Using dynamic light scattering, the hydrodynamic diameter is measured to be  $80.0 \pm 8.5$  nm, in agreement with the TEM measurements and the Mie theory analysis.

**2.2. Second Harmonic Generation.** The second harmonic generation setup is composed of an ultrafast laser system, an optical setup, and a high-sensitivity CCD spectroscopy detector, similar to previously reported experimental set-ups.<sup>48,49</sup> A titanium:sapphire oscillator laser produces 75 fs pulses centered at 800 nm with a repetition rate of 80 MHz and an average power of 2.7 W. The laser beam is focused to a 1 cm quartz cuvette containing the colloidal sample at a diluted concentration of  $3.7 \times 10^8$  nanoparticles/mL in water using a 20 mm focal length lens. An optical filter is placed in front of the cuvette to remove any residual SHG light prior to the sample. Another filter is placed after the sample to remove the fundamental light while transmitting the SHG signal, which is collected in the forward direction and refocused to a monochromator connected to a high-sensitivity spectroscopy

charge coupled device detector. The different dye solutions are added using a computer-controlled buret during automated stirring. Several spectral scans are acquired for each addition of the dye solution, and the isotherms are acquired several times for statistical analysis.

### 3. RESULTS AND DISCUSSION

The spectra containing the SHG signals for each concentration of the added molecular dyes are analyzed to obtain the corresponding adsorption isotherms. For example, Figures 3a,

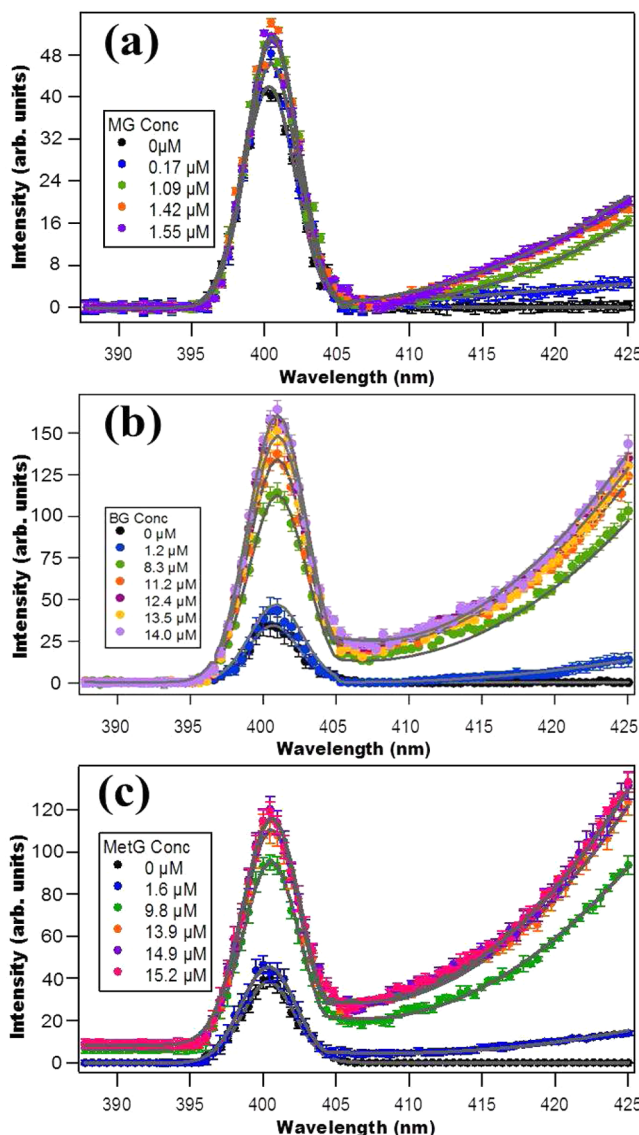


**Figure 3.** Spectra of gold nanoparticles solutions at various (a) malachite green, (b) brilliant green, and (c) methyl green concentrations. The SHG peak is detected near 400 nm.

3b, and 3c display representative spectra obtained at different malachite green, brilliant green, and methyl green concentrations, respectively. The lower wavelength peak is assigned to second harmonic generation while the rise at higher wavelengths is attributed to two-photon fluorescence.<sup>50,51</sup> The spectra are fit using Gaussian functions plus second-order polynomials to represent the SHG and fluorescence signal, respectively, in the measured wavelength range. The corre-

sponding fits all accurately describe the measured spectra, as shown in Figure 3 using solid gray lines, with SHG peaks centered at  $400.5 \pm 0.1$  nm and full width at half-maxima of  $2.5 \pm 0.1$  nm. The peak centers and widths stay constant to within experimental uncertainty for all added dye concentrations. The spectra corresponding to the nanoparticle solution in water without the addition of molecular dyes exhibit SHG signal due mostly to the colloidal nanoparticles. The SHG intensities then increase as the added dye concentrations are increased, reaching maxima as the adsorbates at the gold nanoparticle interface reach their saturation values.

The adsorption isotherms obtained from the SHG results from additions of malachite green, brilliant green, and methyl green to the colloidal gold nanoparticle sample are shown in Figures 4a, 4b, and 4c, respectively. The experimental data are corrected to account for the contribution from hyper-Rayleigh

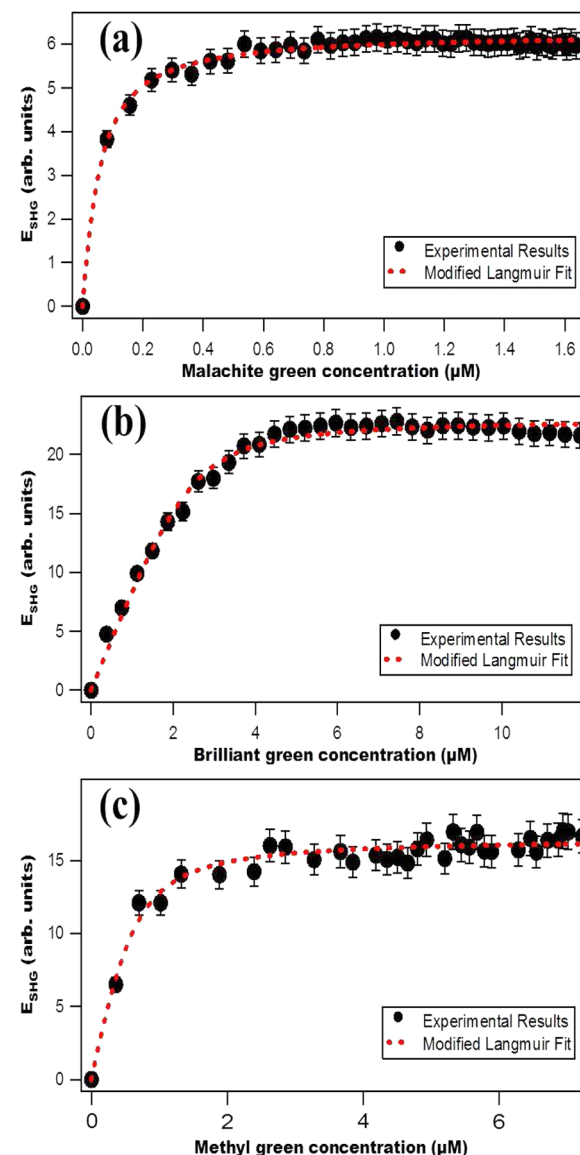


**Figure 4.** Adsorption isotherm results (black dots) obtained from second harmonic generation measurements as a function of (a) malachite green, (b) brilliant green, (c) and methyl green concentrations. The experimental data are compared with the best fits from the modified Langmuir model (dotted red lines).

scattering from the free dye molecules in solution. The hyper-Rayleigh scattering signal as a function of concentration for the three dye solutions is shown in the Supporting Information. More details about this correction method are provided in the Supporting Information. The corrected experimental data are then compared to the modified Langmuir models,<sup>32,48</sup> which includes the depletion of adsorbates from the bulk. The modified Langmuir model is given by

$$\frac{N}{N_{\max}} = \frac{\left(C + N_{\max} + \frac{SS}{K}\right) - \sqrt{\left(C + N_{\max} + \frac{SS}{K}\right)^2 - 4CN_{\max}}}{2N_{\max}} \quad (1)$$

where  $N$  is the adsorbate population on the nanoparticle surface,  $N_{\max}$  is the maximum number of adsorbate sites on the nanoparticle surface multiplied by the concentration of nanoparticles in the solution,  $C$  is the adsorbate bulk concentration added, and  $K$  is the adsorption equilibrium constant.<sup>32</sup> Each adsorption isotherm is analyzed to find the best fit parameters for  $K$  and  $N_{\max}$ . The free energy of adsorption is obtained using the equation,  $\Delta G^\circ = -RT \ln K$ . The maximum number of adsorbate sites on each nanoparticle is determined from  $N_{\max}$  and the known nanoparticle concentration.

The best fits to the measured adsorption isotherms using the modified Langmuir model are shown as red dashed lines in Figure 4. The free energies of adsorption obtained from the best fit parameters for malachite green, brilliant green, and methyl green adsorbing to the colloidal gold nanoparticles are  $-12.5 \pm 0.1$ ,  $-10.0 \pm 0.3$ , and  $-11.1 \pm 0.1$  kcal/mol, respectively. Additionally, the corresponding number of adsorption sites per particle for the three different molecules determined from the best fits are  $(9.18 \pm 0.2) \times 10^3$ ,  $(3.01 \pm 0.2) \times 10^4$ , and  $(1.78 \pm 0.04) \times 10^4$  sites per particle, respectively. This corresponds to adsorption site areas of  $219 \pm 11 \text{ \AA}^2$  for malachite green,  $67 \pm 9 \text{ \AA}^2$  for brilliant green, and  $113 \pm 5 \text{ \AA}^2$  for methyl green, respectively. These results can be understood based on several factors, including adsorbate interactions with the nanoparticle surface as well as adsorbate–adsorbate repulsions. The positively charged molecular dyes all have strong electrostatic attractions to the negatively charged surface. However, the high surface densities of the adsorbates contribute to adsorbate–adsorbate repulsion, which decreases the free energy of adsorption magnitude. Of the three molecules, malachite green has the largest overall free energy of adsorption magnitude while also having the lowest adsorbate site density. Brilliant green has the lowest free energy of adsorption magnitude while consequently having the highest adsorbate site density. Methyl green is doubly charged, leading a stronger electrostatic attraction to the surface as well as greater adsorbate–adsorbate repulsion, and these interactions are counterbalancing. The different molecular structures, especially around the charged nitrogen centers, contribute to different electrostatic potentials at the resulting adsorption site, including the interactions between with the negatively charged carboxylates as well as image-charge attractions with the metal surface.

In addition, the molecular adsorbate tilt angle with respect to the nanoparticle surface is expected to play a key important role in these surface-specific interactions.<sup>52</sup> The SHG signal has been shown previously to depend on the geometrical orientation of the molecules on the nanoparticle surface.<sup>53,54</sup> Here, the signal amplitude of the adsorption isotherm at the

plateau will depend on the tilt angle of the molecular adsorbate. From our measured SHG results, the best fits of the amplitudes from the adsorption isotherms using the modified Langmuir model is  $7.5 \pm 0.1$ ,  $18.4 \pm 0.4$ , and  $23.1 \pm 0.3$  in directly comparable arbitrary units for malachite green, methyl green, and brilliant green using the same nanoparticle sample concentrations described above. These values follow the same trend as  $N_{\max}$  where malachite green has the smallest SHG amplitude and brilliant green has the largest SHG amplitude at the plateau. These SHG signal amplitudes compare to an initial SHG amplitude of  $39.8 \pm 0.8$  for the nanoparticles before adding the dye molecules. The values of the SHG amplitudes and the  $N_{\max}$  values are closely related to the tilt angle, since a smaller tilt angle allows more molecules to be closely packed on the nanoparticle surface. Results for the SHG adsorption isotherms of malachite green, brilliant green, and methyl green to colloidal polystyrene sulfate microparticles are also measured using this setup and are discussed in the Supporting Information, showing excellent agreement with existing literature values.<sup>32</sup>

Comparing these results to previous SHG adsorption isotherm measurements provides a more complete assessment of molecular adsorption to different colloidal nanoparticle samples. The free energies of adsorption of malachite green to 16 nm gold nanoparticles coated in citrate and 1.05  $\mu\text{m}$  polystyrene sulfate microparticles in water have been previously measured to be  $-15.4 \pm 0.4$  and  $-11.1 \pm 0.1$  kcal/mol, respectively, with corresponding adsorbate site areas of  $71 \pm 14$  and  $192 \pm 24 \text{ \AA}^2$ , respectively. Our results indicate that malachite green binds less strongly and with lower site densities to 80 nm gold nanoparticles capped in MSA than to 16 nm gold nanoparticles coated in citrate. It is important to note that MSA forms a tightly bound layer due to the gold–sulfur bond while citrate is only loosely bound to the gold surface. In the gold–citrate surface, malachite green may penetrate the citrate layer and access the gold surface directly to experience a stronger image-charge attraction. For the gold–MSA surface, the tightly bound MSA will increase the separation distance between the adsorbate and the metal surface, leading to a shielding and weakening of the image-charge attraction.<sup>55</sup> However, malachite green has a slightly higher free energy of adsorption and a similar site density on the gold nanoparticles capped in MSA compared with polystyrene sulfate microparticles. By changing the capping agent, the adsorption of molecules to the surface of gold nanoparticles can be significantly altered. The effect of the capping agent on the adsorption properties can be further investigated by performing the same SHG study while changing the capping agent for gold nanoparticle samples of the same size. This has important implications for molecular sensing applications where modifications in the chemical environment of the metal nanoparticle surface can dramatically change the adsorption properties.

In addition to the adsorption properties of molecules to the surface of gold nanoparticles, spectral resonance coupling<sup>35</sup> between the molecules and the plasmonic nanoparticles is observed. Figure 5 shows the extinction spectra of gold nanoparticles in water after the addition of different concentrations of brilliant green and after subtracting the dye spectra at the corresponding concentrations. The corresponding extinction spectra of the gold nanoparticles with malachite green and methyl green are provided in the Supporting Information. A splitting of the plasmonic peak is seen near the molecular excited states. The magnitudes of the newly formed

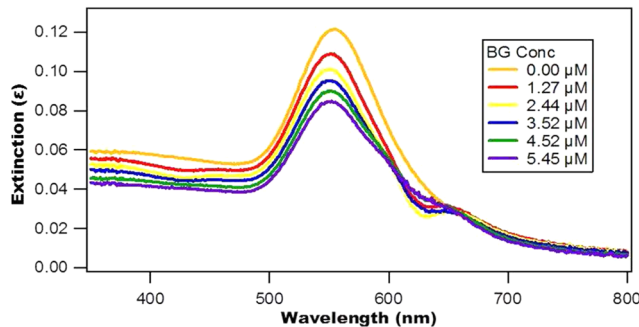


**Figure 5.** Extinction spectra of gold nanoparticles capped with MSA in water at increasing brilliant green concentrations after subtracting the spectra of the dye alone in water at the corresponding concentrations. The 80 nm colloidal gold nanoparticles are initially diluted to  $3.7 \times 10^8$  nanoparticles/mL in water.

peaks increase as the added dye concentrations are increased while the plasmon spectra are depleted, accompanied by wavelength shifts. It is also important to note that the characteristic long wavelength peaks from gold nanoparticle aggregation are not seen in any of these spectra, confirming that gold nanoparticle aggregation is not occurring as the molecular dyes are added.<sup>56</sup> The molecule concentrations are chosen to span the relevant concentrations of the adsorption isotherms determined from the SHG measurements above for each triphenylmethane dye.

From a more careful analysis, the various components of the resonance coupling are determined from the gold nanoparticles interacting with malachite green, brilliant green, and methyl green. Figures 6a–c are obtained after subtracting the extinction spectra of the gold nanoparticles and the dyes alone in water from the ones generated from the mixtures of both at the corresponding concentrations. These figures show the change in the extinction spectra as a result of the molecule–plasmon interactions, including the polariton and Fano-type spectra as well as the plasmon and molecule depletions. Each of these difference spectra are first fit to depletion spectra of the plasmon and molecule to reveal additional peaks that are not from either the plasmon or the molecule, where a positive intensity peak at longer wavelengths and a negative intensity peak at shorter wavelengths are assigned as the  $|P-\rangle$  and  $|P+\rangle$  polaritons, respectively, overlapped with a Fano-type profile. Figures 7a–c show these extra peaks formed for the three dyes compared to the spectra generated from the best fits of the plasmon and molecule depletions. Additional data are reported in the Supporting Information, including the fitting results for the different spectral components. Interestingly, the center wavelengths and full width at half-maxima of the polariton peaks stay relatively constant for each molecule as the concentrations are increased. This indicates that the plasmon–molecule interaction is dominant compared to other possibilities such as dye aggregation,<sup>57</sup> although further experimental and theoretical investigations are needed for a more careful understanding of this effect. The center wavelengths of the  $|P+\rangle$  polaritons for malachite green, brilliant green, and methyl green are  $579 \pm 0.4$ ,  $567 \pm 0.2$ , and  $575 \pm 0.7$  nm, respectively, while the center wavelengths of the  $|P-\rangle$  polaritons are  $655 \pm 0.6$ ,  $664 \pm 0.4$ , and  $670 \pm 1.5$  nm, respectively. The energy difference between the two polariton peaks is assigned to be the Rabi splitting energy,<sup>36</sup> which is determined to be 263, 320, and 306 meV for malachite green,

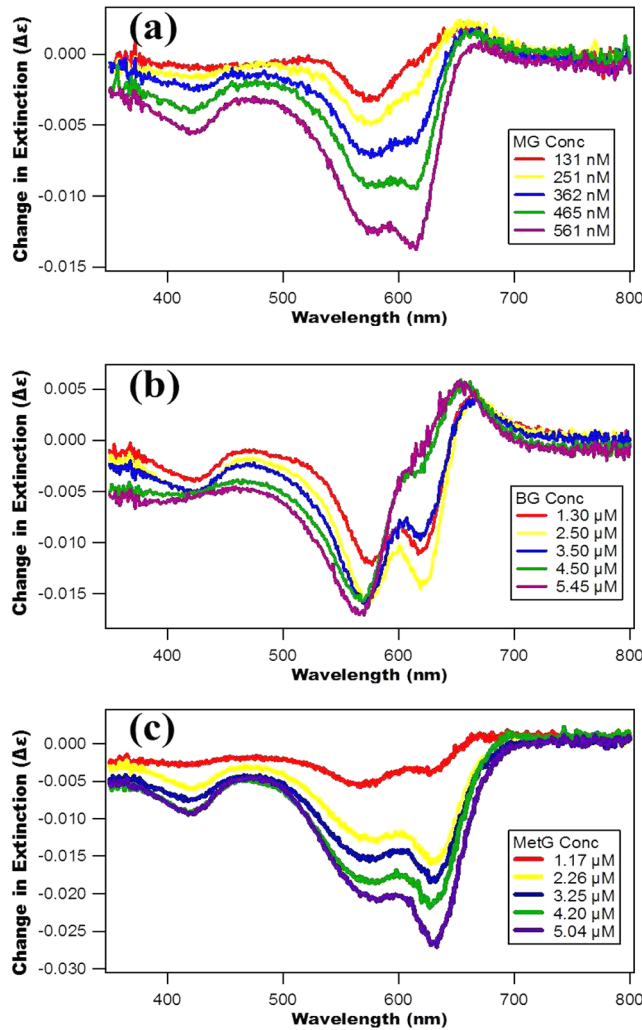


**Figure 6.** Difference spectra obtained from subtracting gold nanoparticle and dye molecule extinction spectra alone in water from the spectra measured from mixtures of both at corresponding concentrations for (a) malachite green, (b) brilliant green, and (c) methyl green.

brilliant green, and methyl green, respectively. These Rabi splitting energies are a measurement of the spectral coupling strengths between molecular excited states and the plasmon resonance and are expected to depend critically on the adsorption tilt angle as well as the quantum mechanical overlaps.

The depletion and polariton intensities are shown in Figure 8 as a function of the dye concentrations. The plasmon depletion intensities exhibit a similar trend for the three different dyes, with increasing depletion as the molecular concentrations are increased. The molecular depletions have different trends with increasing concentrations as part of this signal is due to the molecule being removed from the solution upon adsorption, while another part of this signal is due to the possible plasmonic optical-field enhancements after adsorption. The plasmon depletions, the molecular depletions, and the polariton intensities of the different dye molecules have similar trends when compared to their adsorption properties. Brilliant green has the largest  $N_{\max}$  value and the largest plasmon depletion. Malachite green has the smallest  $N_{\max}$  value and the smallest plasmon depletion. However, malachite green has the largest

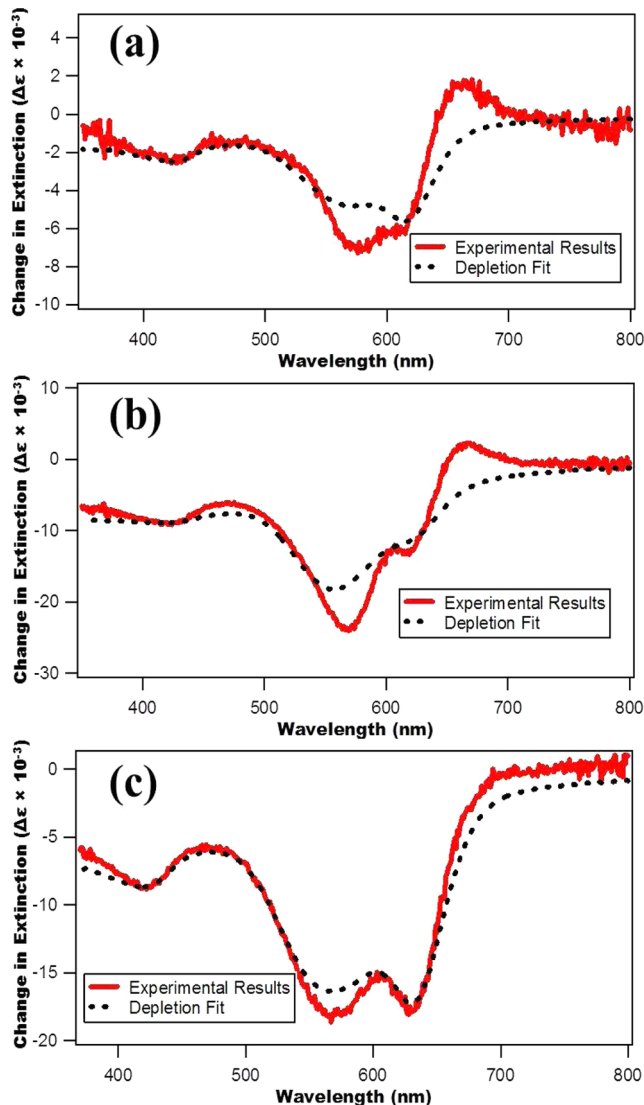


**Figure 7.** Spectral analysis of representative difference spectra from the dye molecules (a) 362 nM malachite green, (b) 3.50  $\mu\text{M}$  brilliant green, and (c) 2.26  $\mu\text{M}$  methyl green interacting with the colloidal gold nanoparticles in water. The residuals show a combination of polariton peaks and Fano-type resonances.

molecular depletion, indicating that it has the lowest level of plasmonic enhancement, possibly due to a large adsorption tilt angle, with the adsorbate lying relatively flat on the surface. Brilliant green has the lowest molecular depletion, the largest Rabi splitting, and the largest polariton intensities, indicating that it has largest relative coupling strength with the plasmonic nanoparticle. Methyl green has intermediate values of molecular depletion, Rabi splitting, and polariton intensities, and it also has an intermediate  $N_{\max}$  value among the three dyes. In addition, the polariton intensities remain somewhat constant as the concentrations are increased, which may occur due to quantum interferences as well as plasmonic interactions with dyes in the bulk solution. Even though malachite green, brilliant green, and methyl green have similar chemical structures and absorption spectra, they exhibit different adsorption properties at the gold nanoparticle surface as well as different spectroscopic interactions from plasmonic–molecular resonance coupling.

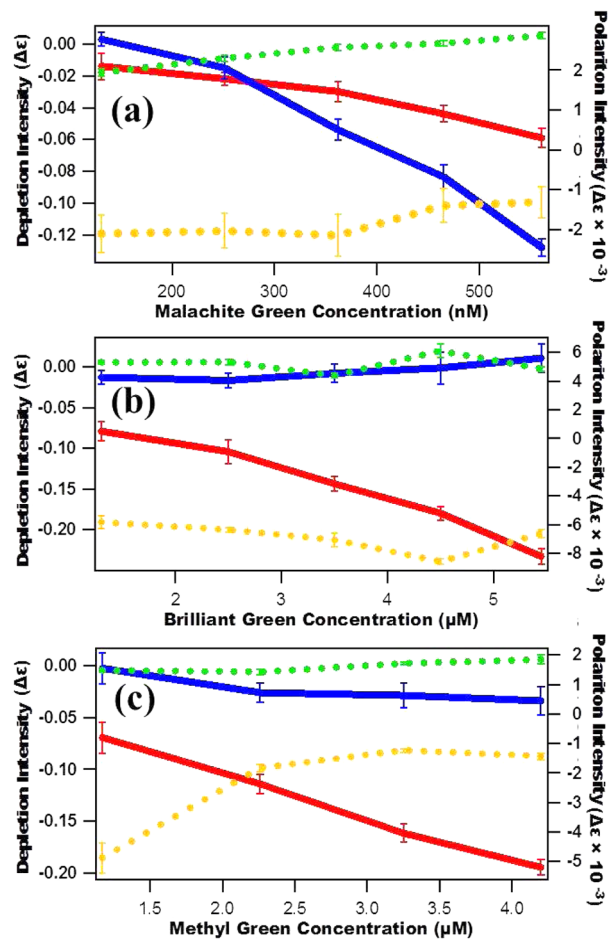


**Figure 8.** Depletion intensities of the plasmon (solid red line) and the molecule (solid blue line) as well as the polariton  $|P-\rangle$  (dashed green line) and  $|P+\rangle$  (dashed orange line) intensities at different (a) malachite green, (b) brilliant green, and (c) methyl green concentrations.

#### 4. CONCLUSION

Second harmonic generation is used to study the adsorption properties of three triphenylmethane dyes to the surface of 80 nm gold nanoparticles capped in mercaptosuccinic acid in aqueous colloidal suspension. The SHG results are analyzed using a modified Langmuir model to determine the free energies of adsorption and the adsorbate site densities at the nanoparticle surface. Malachite green is observed to bind more strongly to the surface of the gold nanoparticles than brilliant green and methyl green but has a lower adsorbate site density. These differences are discussed in terms of the image-charge effect, adsorbate–adsorbate repulsion, and the adsorption tilt angle on the gold nanoparticle surface. Additional comparisons with previous literature results show that malachite green binds less strongly to gold nanoparticles capped with mercaptosuccinic acid than to gold nanoparticles coated with citrate, confirming expectations of weakening image-charge effects due to a tightly bound layer that increases the separation distance between the adsorbates and the metallic surface. Complementary results show plasmonic and molecular resonance coupling as hybrid polaritons and Fano-type profiles are observed using extinction spectroscopy at different molecular concentrations along the adsorption isotherm. Analysis of the spectral changes displays interesting trends involving plasmon

and molecular depletions as well as Rabi splitting energies and polariton intensities that correlate with the SHG adsorption isotherm measurements.

## ■ ASSOCIATED CONTENT

### Supporting Information

More details on the extended modified Langmuir fit, the resonant coupling, and additional figures. This material is available free of charge via the Internet at <http://pubs.acs.org>.

## ■ AUTHOR INFORMATION

### Corresponding Author

\*E-mail lhaber@lsu.edu (L.H.H.).

### Notes

The authors declare no competing financial interest.

## ■ ACKNOWLEDGMENTS

Generous financial support for this work was provided from Louisiana State University. The authors acknowledge Raju Kumal and Emily Harwell for their help in assembling the experimental optical setup. We are grateful to Dr. Raphael Cuerto for his help with the dynamic light scattering measurements and to Dr. Xiaochu Wu for his help with the transmission electron microscope. We would also like to thank Dr. Kenneth Lopata for valuable discussions.

## ■ REFERENCES

- (1) El-Sayed, I.; Huang, X.; El-Sayed, M. Surface Plasmon Resonance Scattering and Absorption of Anti-EGFR Antibody Conjugated Gold Nanoparticles in Cancer Diagnostics: Applications in Oral Cancer. *Nano Lett.* **2005**, *5*, 829–834.
- (2) El-Sayed, I.; Huang, X.; El-Sayed, M. Selective Laser Photo-thermal Therapy of Epithelial Carcinoma Using Anti-EGFR Antibody Conjugated Gold Nanoparticles. *Cancer Lett.* **2006**, *239*, 129–135.
- (3) Kamat, P. V. Photophysical, Photochemical and Photocatalytic Aspects of Metal Nanoparticles. *J. Phys. Chem. B* **2002**, *106*, 7729–7744.
- (4) Narayanan, R.; El-Sayed, M. A. Catalysis with Transition Metal Nanoparticles in Colloidal Solution: Nanoparticle Shape Dependence and Stability. *J. Phys. Chem. B* **2005**, *109*, 12663–12676.
- (5) Haes, A. J.; Van Duyne, R. P. A Nanoscale Optical Biosensor: Sensitivity and Selectivity of an Approach Based on the Localized Surface Plasmon Resonance Spectroscopy of Triangular Silver Nanoparticles. *J. Am. Chem. Soc.* **2002**, *124*, 10596–10604.
- (6) Sperling, R. A.; Gil, P. R.; Zhang, F.; Zanella, M.; Parak, W. J. Biological Applications of Gold Nanoparticles. *Chem. Soc. Rev.* **2008**, *37*, 1896–1908.
- (7) Freddi, S.; D'Alfonso, L.; Collini, M.; Caccia, M.; Sironi, L.; Tallarida, G.; Caprioli, S.; Chirico, G. Excited-State Lifetime Assay for Protein Detection on Gold Colloids–Fluorophore Complexes. *J. Phys. Chem. C* **2009**, *113*, 2722–2730.
- (8) Prigodich, A. E.; Lee, O.-S.; Daniel, W. L.; Seferos, D. S.; Schatz, G. C.; Mirkin, C. A. Tailoring DNA Structure to Increase Target Hybridization Kinetics on Surfaces. *J. Am. Chem. Soc.* **2010**, *132*, 10638–10641.
- (9) Kamat, P. V. Meeting the Clean Energy Demand: Nanostructure Architectures for Solar Energy Conversion. *J. Phys. Chem. C* **2007**, *111*, 2834–2860.
- (10) Link, S.; El-Sayed, M. Shape and Size Dependence of Radiative, Non-radiative and Photothermal Properties of Gold Nanocrystals. *Int. Rev. Phys. Chem.* **2000**, *19*, 409–453.
- (11) Daniel, M.-C.; Astruc, D. Gold Nanoparticles: Assembly, Supramolecular Chemistry, Quantum-Size-Related Properties, and Applications toward Biology, Catalysis, and Nanotechnology. *Chem. Rev.* **2004**, *104*, 293–346.
- (12) Chandra, M.; Dowgiallo, A. M.; Knappenberger, K. L. Controlled Plasmon Resonance Properties of Hollow Gold Nanosphere Aggregates. *J. Am. Chem. Soc.* **2010**, *132*, 15782–15789.
- (13) Stiles, P. L.; Dieringer, J. A.; Shah, N. C.; Van Duyne, R. P. Surface-Enhanced Raman Spectroscopy. *Annu. Rev. Anal. Chem.* **2008**, *1*, 601–626.
- (14) Brus, L. Noble Metal Nanocrystals: Plasmon Electron Transfer Photochemistry and Single Molecule Raman Spectroscopy. *Acc. Chem. Res.* **2008**, *41*, 1742–1749.
- (15) Tam, F.; Goodrich, G. P.; Johnson, B. R.; Halas, N. J. Plasmonic Enhancement of Molecular Fluorescence. *Nano Lett.* **2007**, *7*, 496–501.
- (16) Lakowics, J. R.; Geddes, C. D.; Gryczynski, I.; Malicka, J.; Gryczynski, Z.; Aslan, K.; Lukomska, J.; Matveeva, E.; Zhang, J.; Badugu, R.; et al. Advances in Surface-Enhanced Fluorescence. *J. Fluoresc.* **2004**, *14*, 425–441.
- (17) Baldelli, S.; Eppler, A. S.; Anderson, E.; Shen, Y.-R.; Somorjai, G. A. Surface Enhanced Sum Frequency Generation of Carbon Monoxide Adsorbed on Platinum Nanoparticle Arrays. *J. Chem. Phys.* **2000**, *113*, 5432–5438.
- (18) Bordnyuk, A. N.; Weeraman, C.; Yatawara, A.; Jayathilake, H. D.; Stiopkin, I.; Liu, Y.; Benderskii, A. V. Vibrational Sum Frequency Generation Spectroscopy of Dodecanethiol on Metal Nanoparticles. *J. Phys. Chem. C* **2007**, *111*, 8925–8933.
- (19) Vance, F. W.; Lemon, B. J.; Hupp, J. T. Enormous Hyper-Rayleigh Scattering from Nanocrystalline Gold Particle Suspensions. *J. Phys. Chem. B* **1998**, *102*, 10091–10093.
- (20) Butet, J.; Bachelier, G.; Russier-Antoine, I.; Jonin, C.; Benichou, E.; Brevet, P.-F. Interference between Selected Dipoles and Octupoles in the Optical Second-Harmonic Generation from Spherical Gold Nanoparticles. *Phys. Rev. Lett.* **2010**, *105*, 077401.
- (21) Hao, E. C.; Schatz, G. C.; Johnson, R. C.; Hupp, J. T. Hyper-Rayleigh scattering from silver nanoparticles. *J. Chem. Phys.* **2002**, *117*, 5963–5966.
- (22) Duboisset, J.; Russier-Antoine, I.; Benichou, E.; Bachelier, G.; Jonin, C.; Brevet, P. F. Single Metallic Nanoparticle Sensitivity with Hyper Rayleigh Scattering. *J. Phys. Chem. C* **2009**, *113*, 13477–13481.
- (23) Chandra, M.; Knappenberger, K. L. Nanoparticle surface electromagnetic fields studied by single-particle nonlinear optical spectroscopy. *Phys. Chem. Chem. Phys.* **2013**, *15*, 4177–4182.
- (24) Dadap, J. I.; Shan, J.; Eisenthal, K. B.; Heinz, T. F. Second-Harmonic Rayleigh Scattering from a Sphere of Centrosymmetric Material. *Phys. Rev. Lett.* **1999**, *83*, 4045–4048.
- (25) Eisenthal, K. Second Harmonic Spectroscopy of Aqueous Nano- and Microparticle Interfaces. *Chem. Rev.* **2006**, *106*, 1462–1477.
- (26) Boyd, R. *Nonlinear Optics*; Academic Press: New York, 2010.
- (27) Liu, Y.; Dadap, J.; Zimdars, D.; Eisenthal, K. B. Study of Interfacial Charge-Transfer Complex on TiO<sub>2</sub> Particles in Aqueous Suspension by Second-Harmonic Generation. *J. Phys. Chem. B* **1999**, *103*, 2480–2486.
- (28) Liu, J.; Subir, M.; Nguyen, K.; Eisenthal, K. B. Second Harmonic Studies of Ions Crossing Liposome Membranes in Real Time. *J. Phys. Chem. B* **2008**, *112*, 15263–15266.
- (29) Wang, H.-F.; Troxler, T.; Yeh, A.-G.; Dai, H.-L. Adsorption at a Carbon Black Microparticle Surface in Aqueous Colloids Probed by Optical Second-Harmonic Generation. *J. Phys. Chem. C* **2007**, *111*, 8708–8715.
- (30) Russier-Antoine, I.; Benichou, E.; Bachelier, G.; Jonin, C.; Brevet, P. F. Multipolar Contributions of the Second Harmonic Generation from Silver and Gold Nanoparticles. *J. Phys. Chem. C* **2007**, *111*, 9044–9048.
- (31) Jin, R.; Jureller, J.; Kim, H.; Scherer, N. Correlating Second Harmonic Optical Responses of Single Ag Nanoparticles with Morphology. *J. Am. Chem. Soc.* **2005**, *127*, 12482–12483.
- (32) Wang, H.; Yan, E.; Liu, Y.; Eisenthal, K. B. Energetics and Population of Molecules at Microscopic Liquid and Solid Surfaces. *J. Phys. Chem. B* **1998**, *102*, 4446–4450.

- (33) Yan, E. C. Y.; Liu, Y.; Eisenthal, K. B. New Method for Determination of Surface Potential of Microscopic Particles by Second Harmonic Generation. *J. Phys. Chem. B* **1998**, *102*, 6331–6336.
- (34) Subir, M.; Liu, J.; Eisenthal, K. B. Protonation at the Aqueous Interface of Polymer Nanoparticles with Second Harmonic Generation. *J. Phys. Chem. C* **2008**, *112*, 15809–15812.
- (35) Ni, W.; Chen, H.; Su, J.; Sun, Z.; Wang, J.; Wu, H. Effects of Dyes, Gold Nanocrystals, pH, and Metal Ions on Plasmonic and Molecular Resonance Coupling. *J. Am. Chem. Soc.* **2010**, *132*, 4806–4814.
- (36) Hutchison, J. A.; Liscio, A.; Schwartz, T.; Canaguier-Durand, A.; Genet, C.; Palermo, V.; Samori, P.; Ebbesen, T. Tuning the Work-Function via Strong Coupling. *Adv. Mater.* **2013**, *25*, 2481–2485.
- (37) Cade, N. I.; Ritman-Meer, T.; Richards, D. Strong Coupling of Localized Plasmons and Molecular Excitons in Nanostructured Silver Films. *Phys. Rev. B* **2009**, *79*, 241404(R).
- (38) Sugawara, Y.; Kelf, T. A.; Baumber, J. J.; Abdelsalam, M. E.; Bartlett, P. N. Strong Coupling between Localized Plasmons and Organic Excitons in Metal Nanovoids. *Phys. Rev. Lett.* **2006**, *97*, 266808.
- (39) Hao, F.; Nordlander, P.; Sonnentag, Y.; Van Dorpe, P.; Maier, S. A. Tunability of Subradiant Dipolar and Fano-Type Plasmon Resonances in Metallic Ring/Disk Cavities: Implications for Nanoscale Optical Sensing. *ACS Nano* **2009**, *3*, 643–652.
- (40) Francescato, Y.; Giannini, V.; Maier, S. A. Plasmonic Systems Unveiled by Fano Resonances. *ACS Nano* **2012**, *6*, 1830–1838.
- (41) Luk'yanchuk, B.; Zheludev, N.; Maier, S. A.; Halas, N. J.; Norlander, P.; Giessen, H.; Tow Chong, C. The Fano Resonance in Plasmonic Nanostructures and Metamaterials. *Nat. Mater.* **2010**, *9*, 707–715.
- (42) Lopata, K.; Neuhauser, D. Molecular nanopolaritonics: Cross manipulation of near-field plasmons and molecules. I. Theory and application to junction control. *J. Chem. Phys.* **2007**, *127*, 154715.
- (43) Lopata, K.; Neuhauser, D. Multiscale Maxwell–Schrödinger modeling: A split field finite-difference time-domain approach to molecular nanopolaritonics. *J. Chem. Phys.* **2009**, *130*, 104707.
- (44) Fano, U. Effect of Configuration Interaction on Intensities and Phase Shifts. *Phys. Rev.* **1961**, *124*, 1866–1878.
- (45) Brown, K. R.; Walter, D. G.; Natan, M. J. Seeding of Colloidal Au Nanoparticle Solutions. 2. Improved Control of Particle Size and Shape. *Chem. Mater.* **2000**, *12*, 306–313.
- (46) Perrault, S.; Chan, W. Synthesis and Surface Modification of Highly Monodispersed, Spherical Gold Nanoparticles of 50–200 nm. *J. Am. Chem. Soc.* **2009**, *131*, 17042–17043.
- (47) Jana, N. R.; Gearheart, L.; Murphy, C. J. Evidence for Seed-Mediated Nucleation in the Chemical Reduction of Gold Salts to Gold Nanoparticles. *Chem. Mater.* **2001**, *13*, 2313–2322.
- (48) Haber, L. H.; Kwok, S.; Semeraro, M.; Eisenthal, K. B. Probing the Colloidal Gold Nanoparticle/Aqueous Interface with Second Harmonic Generation. *Chem. Phys. Lett.* **2011**, *507*, 11–14.
- (49) Haber, L. H.; Eisenthal, K. B. Molecular Excited-State Relaxation Dynamics at the Colloidal Microparticle Interface Monitored with Pump–Probe Second Harmonic Generation. *J. Phys. Chem. B* **2013**, *117*, 4249–4253.
- (50) Bhasikuttan, A. C.; Sapre, A. V.; Okada, T. Ultrafast Relaxation Dynamics from the  $S_2$  State of Malachite Green Studied with Femtosecond Upconversion Spectroscopy. *J. Phys. Chem. A* **2003**, *107*, 3030–3035.
- (51) Denk, W.; Strickler, J. H.; Webb, W. W. Two-Photon Laser Scanning Fluorescence Microscopy. *Science* **1990**, *248*, 73–76.
- (52) De Beer, A. G. F.; Roke, S. Sum Frequency Generation Scattering from the Interface of an Isotropic Particle: Geometrical and Chiral Effects. *Phys. Rev. B* **2007**, *75*, 245438.
- (53) Gonella, G.; Dai, H. L. Determination of Adsorption Geometry on Spherical Particles from Nonlinear Mie Theory Analysis of Surface Second Harmonic Generation. *Phys. Rev. B* **2011**, *84*, 121402(R).
- (54) Lakowicz, J. R. Radiative Decay Engineering 5: Metal-Enhanced Fluorescence and Plasmon Emission. *Anal. Biochem.* **2005**, *337*, 171–194.
- (55) Brüesch, P.; Christen, T. The Electric Double Layer at a Metal Electrode in Pure Water. *J. Appl. Phys.* **2004**, *95*, 2846–2856.
- (56) Vance, F. W.; Lemon, A. B. L.; Hupp, J. T. Enormous Hyper-Rayleigh Scattering from Nanocrystalline Gold Particle Suspensions. *J. Phys. Chem. B* **1998**, *102*, 10091–10093.
- (57) Spano, F. C. The Spectral Signatures of Frenkel Polarons in H- and J-Aggregates. *Acc. Chem. Res.* **2010**, *43*, 429–439.